2024 IEEE/RSJ International Conference on Intelligent Robots and Systems (IROS)
October 14-18, 2024. Abu Dhabi, UAE

Small Multi-Rotor UAV Oriented Direct Thrust Sensor Based on Lightweight Barometers

Han Jiang, Yanchun Chang, Liying Yang, and Yuqing He, *Member, IEEE*

***Abstract*—The multirotor unmanned aerial vehicle (UAV) requires precise control over thrust output when operating in wind-disturbed environments or executing intricate flight missions. Although current commercial force sensors offer high sensitivity and accuracy, they are often heavy and costly. These characteristics restrict their applicability in weight-sensitive and cost-sensitive scenarios, such as thrust measurement in UAVs. To overcome this difficulty, we have developed an embedded barometric force sensor (BFS) that mounts between the UAV's airframe and motor, allowing direct measurement of the force exerted by the rotor on the UAV's rigid body. The BFS is designed using low-cost MEMS barometers as tactile force sensors, encased in polyurethane rubber. Subsequently, we established its parameter model and devised a stability improvement strategy to reduce the impact of temperature. Additionally, we designed a structure suitable for mounting the BFS on the UAV to safeguard the rubber module from damage and reconstructed the thrust model to account for the impact of weight and friction on thrust measurement. Finally, we assembled testing platforms to validate the performance of the BFS. Experimental results demonstrate the BFS's excellent linearity, wide range, adequate bandwidth to respond to UAV thrust variations, and confirm the feasibility of mounting the BFS on the UAV for thrust measurement and force feedback control.**

I. Introduction

Multirotor unmanned aerial vehicles (UAVs) are extensively utilized in various domains including search and rescue operations, military applications, plateau scientific investigations, and more [1]-[2]. Moreover, as UAV control technology advances, research is increasingly focused on enhancing complexity, precision, and robustness. For instance, ensuring precise control of output thrust becomes crucial for UAVs navigating through wind-disturbed environments or executing rapid obstacle avoidance maneuvers [3]-[5].

To derive rotor thrust, researchers have endeavored to develop a mathematical model based on aerodynamic theory. Bangura and Mahony developed an intricate rotor thrust model, leveraging an aerodynamic power model from a fixed-pitch rotor. They integrated this model with a motor power sensor and estimator to calculate rotor thrust [6], [7]. However, this model necessitated the computation of numerous parameters. Consequently, researchers proposed a simplified parametric model for rotor thrust, derived through extensive experimentation [8]-[10]. Furthermore, in order to attain a more accurate lift and drag coefficient model, researchers conducted wind tunnel experiments to the specific blade [11], [12]. However, variations in both the size and material of the blades impact the calculation of lift and drag coefficients, consequently diminishing the accuracy of the rotor thrust model and leading to deviations between calculated and actual thrust values.

An alternative effective approach involves directly measuring rotor thrust. Moreover, this method can be categorized into utilizing strain gauges or force sensors. Regarding the direct measurement of thrust using strain gauges, [13] proposed a method to measure the true forces on the motor beams for each tilt motor employing dedicated hardware that mounts the strain gauges on the torque rod. The approach employed a full-bridge Wheatstone circuit and electrical resistance strain gauges, combined with constant-stress cantilever beams, for rotor thrust measurement [14]. Kamp and Gong introduced a lightweight, accurate in-flight thrust measurement system designed for multirotor UAVs, utilizing strain gauges [15], [16]. Nevertheless, direct force measurement using strain gauges is plagued by high frequency and a high noise-to-signal ratio, rendering it unsuitable for rotor thrust measurement [17].

Using commercial force sensors can directly measure thrust, but their weight and cost limitations restrict their use in weight-sensitive and cost-sensitive applications [18]. To overcome this challenge, Tenzer proposed a novel approach to constructing tactile array sensors using barometric pressure sensor chips and standard printed circuit boards (PCBs). This method utilizes low-cost MEMS barometers encased in polyurethane rubber to serve as tactile force sensors [19]. These tactile sensors are not only low-cost and easy to fabricate but also lightweight. In the literature [20], [21], and [22], this method has been applied to robotic hands for tasks such as localizing contact, estimating normal force, and identifying object shapes. Additionally, a unified solution was proposed for three-axis force and contact angle measurement based on this approach [23]. To adapt this technique for UAVs, Davis designed a circular barometric tactile array sensor mounted under the motor to directly measure rotor thrust [24], [25]. However, the measurement range of the sensor is small (just 0.5 N), and it does not account for the effect of temperature on the rubber.

*This work was supported by the National Key Research and Development Program of China under Grants 2022YFC3005104, in part by the National Natural Science Foundation of China Joint Fund Key Project U22B2041, in part by the Youth Innovation Promotion Association of the Chinese Academy of Sciences under Grant Y2022065, in part by the National Natural Science Foundation Youth Fund 62303448.

Han Jiang is with the State Key Laboratory of Robotics, Shenyang Institute of Automation, Chinese Academy of Sciences, Shenyang 110016, China, with the Institutes for Robotics and Intelligent Manufacturing, Chinese Academy of Sciences, Shenyang 110016, China, and also with the University of Chinese Academy of Sciences, Beijing 100049, China (e-mail: jianghan@sia.cn).

Yanchun Chang, Liying Yang and Yuqing He are with the State Key Laboratory of Robotics, Shenyang Institute of Automation, Chinese Academy of Sciences, Shenyang 110016, China, and also with the Institutes for Robotics and Intelligent Manufacturing, Chinese Academy of Sciences, Shenyang 110016, China (e-mail: changyanchun@sia.cn; yangliying@sia.cn; heyuqing @sia.cn).

To ensure that the measurement range of the barometric force sensor (BFS) aligns with the load requirements of each individual motor, we conducted an analysis of the relationship between the design parameters of the rubber module and pressure, subsequently establishing a mathematical model for force. For enhancing measurement stability, we implemented a strategy to mitigate the impact of temperature fluctuations. To achieve direct measurement of rotor thrust and safeguard the BFS from potential damage, we devised a structure suitable for mounting the BFS between the airframe and motor of the UAV. Additionally, we revised the thrust model to incorporate the effects of weight and friction on thrust measurement. Furthermore, we constructed testing platforms to validate the BFS's excellent linearity and adequate bandwidth, ensuring it meets the basic requirements for UAV thrust variation. Lastly, we established a single-axis dynamical system to verify the feasibility of integrating the BFS into the UAV for thrust measurement and force feedback control. The primary contributions of this study are summarized as follows.

1) We develop a direct force measurement sensor tailored for multi-rotor UAVs and investigate the influence law of temperature, friction, and the weight of the mounting structure on measurement accuracy and stability.

2) We validate that the sensor's system bandwidth is adequate to fulfill the frequency requirements for UAV thrust variation.

3) We establish a single-axis dynamical system and perform closed-loop tests to confirm the stability and accuracy of force output, as well as the feasibility of implementing force feedback control on the UAV.

The remainder of this paper is organized as follows. Section II describes the construction of the BFS, analyzes the force measurement principle of the BFS in detail, establishes its parameter model, and designs the stability improvement strategy. Section III explains the structural design of the BFS mounted on the UAV, rebuilds the force model, and introduces the force feedback control system based on the BFS. Section IV discusses experimental results, and Section V presents conclusions and future work.

II. Barometric Force Sensor Design

A. Construction

The barometric force sensor (BFS) consists of eight barometers, an STM32 microcontroller, a serial port module, and other essential components mounted on a printed circuit board (PCB). The barometer employed is the MPL115A2 pressure sensor, chosen for its relatively large ventilation hole (1 mm diameter) directly above the pressure sensor, which facilitates rubber casting [19]. An appropriate spatial configuration ensures that the barometer can provide reliable signals in response to the applied load. A desirable approach is to configure the structure as a series of modules, each comprising a rubber block with two embedded barometers symmetrically distributed along the z-axis. To evenly distribute the applied load across each rubber module, an acrylic load plate is designed for easy mounting on top of the polyurethane-encased pressure sensor. To securely mount the BFS between the airframe and motor of the UAV, equally sized through-holes are

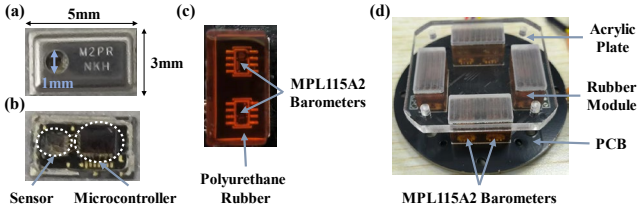

Fig. 1. (a) MPL115A2 barometer (5mm×3mm); (b) Barometer showing with casing removed; (c) The rubber module; (d) Barometric force sensor.

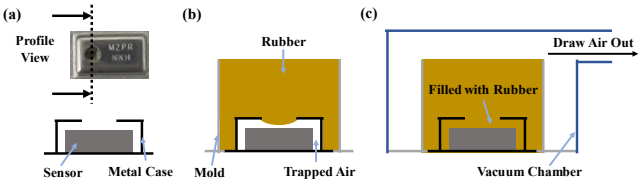

Fig. 2. (a) Profile view of the MPL115A2 barometer; (b) Air is trapped inside the barometer after completion of pouring; (c) Draw trapped air out in the vacuum chamber to fill the interior of the barometer with rubber.

punched in the PCB and acrylic plate for screw fastening. The completed BFS, depicted in Fig. 1, has a mass of 50g, with a total materials cost per sensor approximately $55.

B. Rubber Casting

Commercial barometers are unable to directly measure tactile force. However, embedding barometers into rubber enables them to measure contact force. The chosen rubber type is Smooth-on VytaflexTM 20 polyurethane, known for its superior physical and performance properties [19], [24]. To facilitate better molding of the polyurethane rubber over the barometers, a mold was crafted from acrylic using a milling machine and secured to the PCB using bolts and nuts. Prior to pouring the rubber, a thin layer of petroleum jelly was applied to the mold to serve as a release agent. Subsequently, the liquid polymer is poured into the mold and allowed to cure, forming the elastomer contact surface. It is important to note that pouring the rubber at normal atmospheric pressure may result in the trapping of air inside the barometer cavity, potentially reducing the sensitivity and resolution of the BFS [18]. A successful approach involves vacuum degassing the BFS immediately after pouring, as depicted in Fig. 2.

C. Force Model

The BFS measures normal stress in the direction perpendicular to the chip package, with minimal response to shear stresses. This characteristic is well-suited for measuring rotor thrust, as the thrust generated by the motor acts in the normal direction. Considering the spatial arrangement of the rubber modules and their MEMS barometers, a mechanical analysis can establish a connection between the force applied to the acrylic plate and the local loads on the barometers, based on the geometric design parameters. The principle underlying the force measurement of the BFS is to convey surface contact pressure within the rubber layer to the ventilation hole, and subsequently to the MEMS barometer. More specifically, when a downward normal force is applied at the center of the acrylic plate, the rubber modules undergo compression de-

formation with uniform compression. Consequently, size equal and reversed interacting normal internal forces are generated between the different parts within the rubber modules. As the barometer is a MEMS piezoresistive strain pressure sensor, it measures the applied pressure through a sensing element consisting of a silicon diaphragm with a piezoresistive strain bridge. Subsequently, this change is converted by the MEMS element into a modification in the barometer output values (pressure ADC), thereby indicating a change in the normal internal force. Consequently, it is essential to model the relationship between barometer output values and the internal force. A purely normal load applied to the acrylic plate is transmitted to the rubber modules, resulting in uniform uniaxial compression, as depicted in Fig. 3(a). Therefore,

$$\sigma_z = \frac{F_z}{4(LW-(4-\pi)R^2)}, \tag{1}$$

where σ_z represents the normal stress on the barometer, F_z is the normal force, L denotes the length of each rubber module, W stand for the width of each rubber module, and R is the fillet radius of each rubber module (designed with fillet to facilitate the mold processing and demolding), as illustrated in Fig. 3(b). Subsequently, a coefficient K_1 is introduced to represent the units of pressure ADC count per unit stress, establishing the relationship between barometer output and stress. The relationship between barometer output and loads is

$$P_{ADC} = \frac{K_1 F_z}{4(LW-(4-\pi)R^2)} + P_{ADC0}, \tag{2}$$

where P_{ADC} represents the pressure ADC count of the barometer, and P_{ADC0} is the initial pressure ADC count. Finally, we define the total response by combining the counts of eight barometers, expressed as

$$F_z = \frac{LW-(4-\pi)R^2}{2K_1}\sum_{i=1}^{8}(P_{ADCi}-P_{ADC0i}). \tag{3}$$

Equation (3) directly relates the design parameters of the rubber module to the barometer output and can be utilized to optimize the configuration for a desired resolution and range.

D. Stability Improvement Strategy

The rubber module affects the BFS's measurement stability in two ways. One factor is the presence of trapped air, illustrated in Fig. 2, which has been addressed through vacuum degassing [19]; the other is temperature fluctuations, where minor changes result in significant variations in readings.

During operation, the BFS's temperature increases when power is applied, leading to the expansion of the rubber. Nevertheless, the metal casing of the barometer restricts its internal space, thereby casing insufficient room for the rubber to expand outward. Additionally, due to the incompressible nature of the polyurethane rubber, it squeezes the sensing element, resulting in a rapid increase in the pressure ADC count of the barometer. Consequently, this reduces the barometer's range and diminishes the measurement stability.

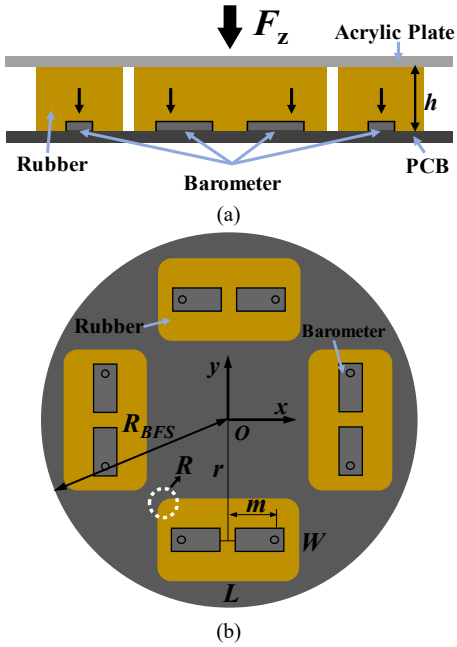

Fig. 3. (a) Side view of the BFS; (b) Top view of the BFS.

To mitigate this issue, we removed the metal casing of the MPL115A2 barometer to expose the MEMS pressure sensor directly, effectively allowing for sufficient space for rubber expansion. However, the barometer itself causes the pressure ADC count to fluctuate with temperature changes. Thus we simultaneously read the pressure and temperature ADC counts, combined with the temperature compensation method [26]:

$$P_{COMP} = a_1 + (b_1 + c_1 \cdot T_{ADC}) \cdot P_{ADC} + d_1 \cdot T_{ADC}, \tag{4}$$

where a_1, b_1, c_1, d_1 are the system coefficients of the barometer, typically stored in the host microcontroller's local memory but retrievable at any time; P_{ADC} is the pressure ADC count, T_{ADC} is the temperature ADC count, and P_{COMP} is the compensated pressure value. In accordance with equation (4), we consider the compensated pressure value as the barometer's output. Combined with (3), the normal load F_z is redefined as

$$F_z = \frac{LW-(4-\pi)R^2}{2K_2}\sum_{i=1}^{8}(P_{COMPi}-P_{COMP0i}), \tag{5}$$

where K_2 is units of P_{COMP} per unit stress, P_{COMPi} is the compensated pressure value of the i-th barometer, and P_{COMP0i} is the initial compensated pressure value of the i-th barometer.

III. The Application of the BFS on the UAV

A. Mounting Structure

The rubber modules of the BFS adhere to the PCB through adhesion. Excessive pulling force may cause these rubber modules to detach from the PCB. Consequently, we designed a mounting structure to convert the pulling force generated by the rotor into compression force, which mounts the BFS upside down, as depicted in Fig. 4. The total weight of the mounting structure and BFS is 120g.

In the described structure, the rotor, motor, and connecting plate are fastened together with screws, while the acrylic plate

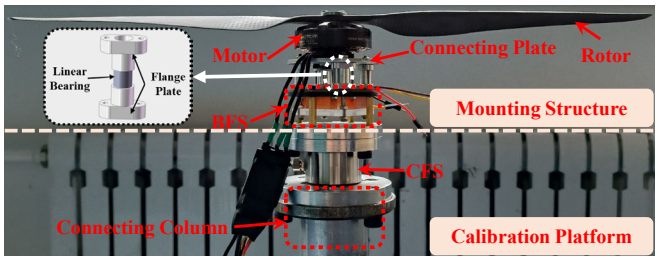

Fig. 4. The upper part is the mounting structure suitable for measuring the thrust generated by the rotor, and the lower part is the sensor calibration platform containing the CFS and connecting column.

is linked to the connecting plate using stud bolts. When the rotor rotates, it generates thrust, causing the connecting plate to pull the acrylic plate upward via the stud bolts. This action compresses the rubber modules, leading to a change in the BFS reading. Nevertheless, the rotation of the rotor generates both thrust and torque simultaneously. This torque tilts the stud bolts, constraining the vertical movement of the acrylic plate and consequently leading to inaccurate thrust measurements by the BFS. Consequently, we utilize linear bearings to limit the lateral movement of the stud bolts and ensure smooth vertical movement, thereby counteracting the torque exerted on the stud bolts.

B. Force Analysis

a). Effect of Weight on Thrust Measurement

The four flange plates bear the total weight M of the rotor, motor, connecting plate, stud bolts, and acrylic plate while stationary. The thrust generated by the rotor is denoted as T, when $0 \le T \le M$, the connecting plate and flange plates are in a snug state, and the acrylic plate does not compress rubber modules; when $T > M$, the connecting plate separates from flange plates, causing the acrylic plate to compress the rubber modules and resulting in a change in the BFS reading. To illustrate the aforementioned process more visually, refer to the schematic diagram shown in Fig. 5.

b). Effect of Friction Force on Thrust Measurement

The rotation of the rotor also generates torque M_z. for each stud bolt an equivalent force $F=M_z/4d$ is applied, where d is the distance from the center of the stud bolt to the coordinate origin. Additionally, the rotation of the rotor generates thrust. The stud bolts pull the acrylic plate vertically upward, while simultaneously generating a vertically downward friction force f, as depicted in Fig. 5(b).

Because of the large number of balls within the linear bearings, rolling friction occurs between linear bearings and stud bolts. The rolling friction force is defined as

$$f = \frac{n\mu}{r} \cdot F = \frac{n\mu}{4rd} \cdot M_z , \tag{6}$$

where μ is the rolling friction coefficient, n is the number of balls, r is the radius of the ball; thrust T and torque M_z generated by the rotor are approximately linearly related, that is

$$M_z = \alpha \cdot T , \tag{7}$$

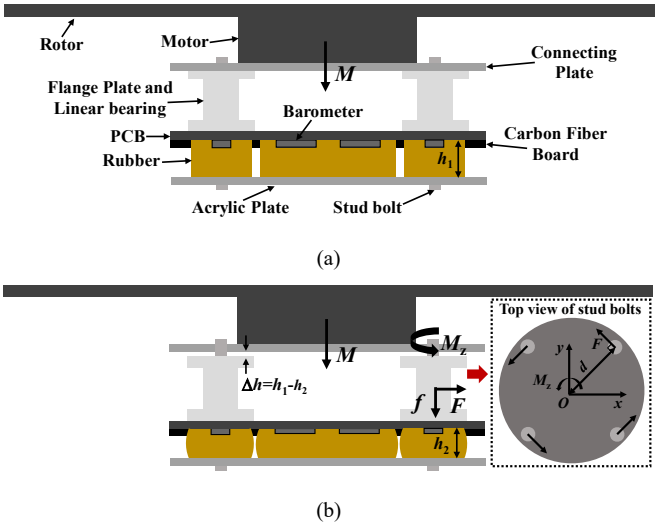

Fig. 5. (a). Schematic diagram of the BFS operation in the state $0 \le T \le M$; (b). Schematic diagram of the BFS operation in the state $T > M$, and representation of the friction force acting on stud bolts.

where α denotes the fitting coefficient, combined with (6), the rolling friction force is rewritten as

$$f = \frac{n\mu\alpha}{4rd} \cdot T . \tag{8}$$

c). Solving for Thrust T

Based on the preceding analysis, the reading of the BFS can be influenced by both the weight M and friction f. Thus the actual thrust T generated by the rotor is expressed as

$$T = F_{BFS} + f + M , \tag{9}$$

where F_{BFS} is the force calculated by the BFS, combined with (5) and (8), (9) can be written in its entirety as

$$T = \frac{4rd}{4rd - n\mu\alpha} \cdot \frac{LW - (4-\pi)R^2}{2K_2} \cdot \sum_{i=1}^{8} (P_{COMPi} - P_{COMP0i}) + \frac{4rd}{4rd - n\mu\alpha} \cdot M , \tag{10}$$

let

$$a = \frac{4rd}{4rd - n\mu\alpha} \cdot \frac{LW - (4-\pi)R^2}{2K_2} , b = \frac{4rdM}{4rd - n\mu\alpha} ,$$

$$P_{BFS} = \sum_{i=1}^{8} (P_{COMPi} - P_{COMP0i}) ,$$

equation (10) is simplified to a linear function that correlates with the reading of the BFS

$$T = a \cdot P_{BFS} + b . \tag{11}$$

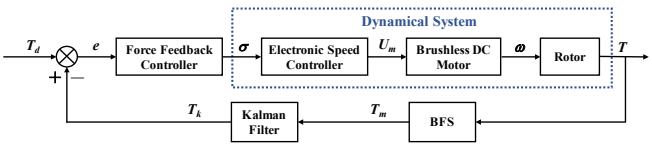

Fig. 6. Force feedback control system.

TABLE I

RELEVANT PARAMETERS SETTING

	Value (mm)		Value (mm)
h	10	L	20
W	10	R	1
m	4	r	17
d	24.5	R_{BFS}	33

TABLE II

MEAN OF SENSOR READINGS AT DIFFERENT MOTOR SPEEDS

Motor Speed (RPM)	P_{BFS} of BFS	Measurement Value of CFS (N)	T_{BFS} of BFS (N)
3000	54.4	5.687	5.624
3250	70.6	6.531	6.584
3500	88.7	7.851	7.653
3750	99.8	8.408	8.316
4000	135.1	10.283	10.405

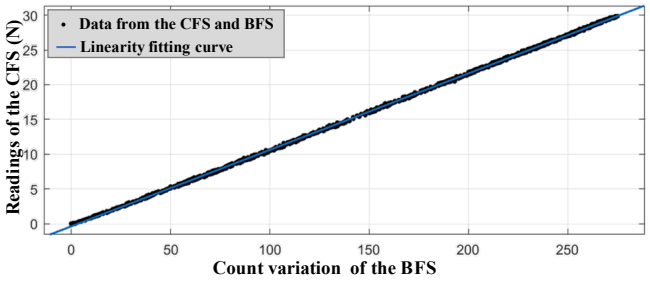

Fig. 7. Linearity fitting situation of the BFS.

C. Force Feedback Control System Based on the BFS

To provide a clearer depiction of the force feedback control system, a control block diagram is depicted in Fig. 6. In this diagram, T_d represents the desired thrust output by the flight controller, T_m signifies the thrust measured by the BFS, T_k denotes the thrust after Kalman filtering to minimize the effect of high-frequency and white noise on the control system, $e = T_d - T_k$ stands for the difference between the desired thrust and actual thrust, σ represents the thrust control quantity, U_m corresponds to the equivalent DC voltage output to the motor, ω denotes the motor speed, and T is the thrust generated by the rotor. Initially, the flight controller outputs T_d and differences with T_k to obtain e, serves as the input of the force feedback controller. In this system, we employ a PID controller as the force feedback controller. Subsequently, the thrust control quantity σ serves as the input of the dynamical system comprising the electronic speed controller, brushless DC motor, and rotor to control T. Finally, the thrust T is regulated by the force feedback control system to achieve the desired thrust T_d.

IV. EXPERIMENTS

Prior to conducting the experiment, relevant parameter settings were provided, as depicted in Table I.

A. Thrust Model Calibration

Within the thrust model (11), coefficients a and b remain to be determined, necessitating sensor calibration. To fulfill this objective, a sensor calibration platform was constructed, as depicted in Fig. 4. Rotation of the rotor generates equal thrust on both the BFS and CFS. Thus, by adjusting the motor speed to generate varying thrust magnitudes and calibrating coefficients a and b using the CFS readings as reference values.

According to the analysis in Section III-B, the sensor registers a change in reading only when the thrust exceeds the total weight. Consequently, calibration experiments were conducted by varying the motor speed within the range of 3000 to 4000 rpm, incremented by 250 rpm. Referring to Table II, where the second column corresponds to the BFS readings P_{BFS} and the measurement values of the CFS serve as the actual thrust T for solving a and b. After calculation, $a = 0.059$ and $b = 2.396$. Next, T_{BFS} was calculated based on P_{BFS}, yielding $T_{BFS} = 0.059 \cdot P_{BFS} + 2.396$, as indicated in the contents of the fourth column. By comparing the thrust values in the third and fourth columns, it is evident that the maximum deviation of the average values between the two sensors is less than 0.2N, signifying the efficacy of the calibrated coefficients. Subsequent experiments were conducted based on these results.

B. Performance of the BFS

a). Linearity

To assess the linearity of the BFS, we conducted a linearity evaluation experiment, in which a commercial force sensor (CFS) was used as a reference. To mitigate the impact of temperature on the experiment, we conducted the linearity evaluation in a controlled indoor environment maintained at a constant temperature. The counts of the BFS were taken as the horizontal axis, and the readings of the CFS were taken as the vertical axis to plot the scatter plot of the applied force. A linear function was employed to assess the linearity of the BFS. The slope of the function is 0.11, indicating that each pressure ADC count corresponds to a force of 0.11N. Fig. 7 illustrates the linearity fitting of the BFS and its measurement range. The results exhibit highly linear behavior, with a coefficient of determination of $r^2 = 0.9998$, and a measurement range exceeding 30N. Thus, BFS demonstrates excellent linearity and a large measurement range.

b). Thermal Behavior

To verify the effectiveness of the stability improvement strategy, a new sensor was developed with one barometer removed the metal case (Barometer-I) and the other barometer retained its metal case (Barometer-II) in a separate rubber module, as shown in Fig. 8.

Employing model (5), it was determined that the resolution of the compensated pressure value P_{COMP} is 0.05N per count. The resolution of the pressure ADC count P_{ADC} is 0.11N per count. After unloading the sensor, it was placed in the temperature box, and the temperature was gradually increased from 20℃ to 25℃. During this process, the readings of Barometer-I and Barometer-II changed. Because Barometer-I was de-cased, the rubber comes into full contact with its MEMS chip.

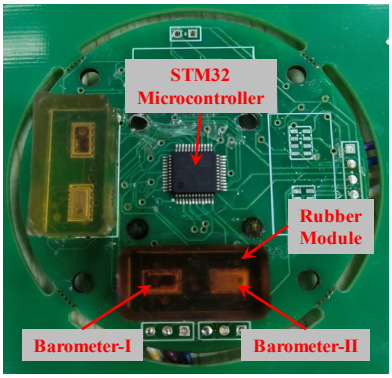

Fig. 8. Sensor used to verify the effectiveness of the strategy.

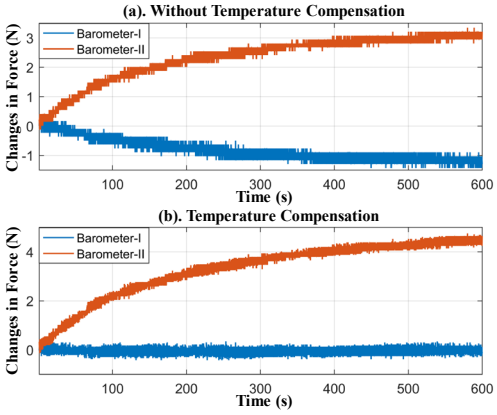

Fig. 9. (a) Barometer readings without temperature compensation; (b) Barometer readings with temperature compensation.

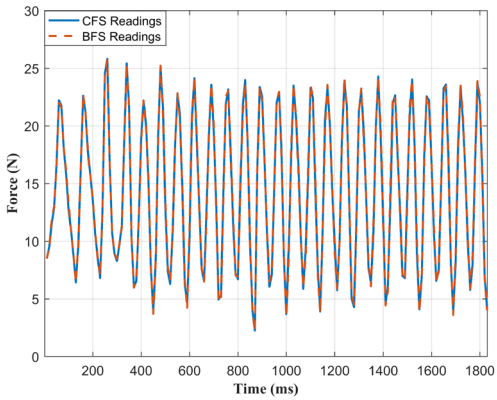

Fig. 10. The CFS and BFS readings at 20Hz frequency.

TABLE III

DATA ANALYSIS OF THE BAROMETER READINGS WITHOUT TEMPERATURE COMPENSATION

	Maximum(N)	Minimum(N)	Mean(N)	Variance
Barometer-I	0.167	-1.433	-0.844	0.131
Barometer-II	3.339	-1.27	2.324	0.565

TABLE IV

BAROMETER READING WITH TEMPERATURE COMPENSATION

	Maximum(N)	Minimum(N)	Mean(N)	Variance
Barometer-I	0.345	-0.432	-0.057	0.011
Barometer-II	4.75	-0.139	3.292	1.239

As the temperature increased, the rubber expanding with heat, simultaneously pulled the pressure-sensitive membrane of Barometer-I to expand outward. Consequently, Barometer-I was subjected to tension, which resulted in a decrease in reading, as depicted by the blue curve in Fig. 9(a). In contrast, the metal case of Barometer-II restricts the expansion of the rubber. The limited space prevented the rubber from expanding outward, thus forcing it to compress the pressure-sensitive membrane of Barometer-II inward. Consequently, Barometer-II experienced pressure, resulting in an increase in the reading, as illustrated by the orange curve in Fig. 9(a). According to Table III, compared to Barometer-II, Barometer-I exhibits 65.29% less fluctuation in readings, with the mean decreasing by 63.68%, and a 76.81% reduction in variance. Therefore, Barometer-I is less susceptible to temperature variations, and removing the metal case of the barometer can mitigate the impact of temperature on readings. Fig. 9(b) illustrates that readings of Barometer-I exhibit greater stability with no significant deviation in the curve, as depicted by the blue curve. According to Table IV, Barometer-I demonstrates significantly smaller range, mean, and variance of readings compared to Barometer-II. Specifically, for the Barometer-I, the application of temperature compensation has led to a reduction in the fluctuation range of readings by 51.44%, a decrease in the mean by 93.25%, and a 91.61% reduction in variance compared to results without temperature compensation. Thus, the temperature compensated barometer exhibits superior performance. In conclusion, removing the metal case of the barometer and implementing temperature compensation as per (4) prove effective in enhancing stability and accuracy.

c). Bandwidth

In prior work, we identified the model of the rotor UAV dynamical system, mapping the electronic speed controller input (PWM) to thrust (T), and determined a system bandwidth of 18Hz. Therefore, we conducted a bandwidth testing platform to validate the bandwidth of the BFS. The platform comprises a CFS (SBT673, bandwidth exceeding 200Hz, price $500, mass 250g), BFS, and vibration table. The vibration table supplies vibrations at a fixed frequency and consistent amplitude. The vibration table amplitude was set to 0.5mm, and fixed-frequency vibration experiments ranging from 1Hz to 20Hz were conducted. The frequency was incremented by 1Hz every 2 seconds until reaching 20Hz. Generally, a higher system bandwidth frequency allows for better responsiveness to low frequency signals. Consequently, a comparison of the CFS and BFS readings at a frequency of 20Hz was conducted, as illustrated in Fig. 10. The results demonstrate that the BFS accurately tracks the force, comparable to the substantially costlier CFS measurements. Therefore, the BFS bandwidth exceeds or equals 20Hz, meeting the measurement demands for UAV force variations.

C. Key Factors Affecting Sensor Measurement Accuracy

According to the analysis mentioned above, temperature, weight M ,and friction force f significantly affect the measurement accuracy and stability of BFS.

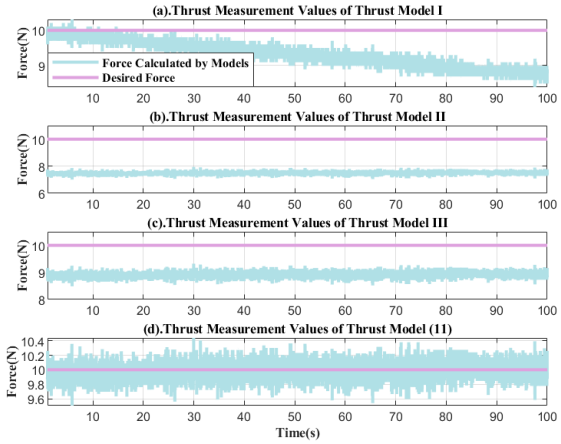

Fig. 11. Thrust measurement values of thrust models I, II, III, and (11).

TABLE V

THE ANALYSIS OF THRUST MEASUREMENT VALUES

Thrust Model	Mean (N)	Variance	Error (%)
I	9.33	0.13	6.7
II	7.49	0.1	25.1
III	8.91	0.1	10.9
(11)	9.98	0.1	0.2

To explore the influence law of different factors on measurement accuracy and stability, a validation experiment was designed using the control variate method. Firstly, perform weight and friction force compensation for the thrust model, without temperature compensation, and the thrust model I is presented as

$$T = \frac{4rd}{4rd - n\mu\alpha} \cdot \frac{LW - (4-\pi)R^2}{2K_2} \cdot \sum_{i=1}^{8}(C_i - C_{0i}) + \frac{4rdM}{4rd - n\mu\alpha};$$

Then, perform temperature and friction force compensation for the thrust model, without weight compensation, and the thrust model II is given by

$$T = \frac{4rd}{4rd - n\mu\alpha} \cdot \frac{LW - (4-\pi)R^2}{2K_2} \cdot \sum_{i=1}^{8}(P_{COMPi} - P_{COMP0i});$$

Next, perform temperature and weight compensation for the thrust model, without friction force compensation, and the thrust model III is represented as

$$T = \frac{LW - (4-\pi)R^2}{2K_2} \cdot \sum_{i=1}^{8}(P_{COMPi} - P_{COMP0i}) + M;$$

Finally, the thrust measurement experiment was conducted with the desired thrust 10N including thrust models I, II, III, and (11).

Fig. 11 records thrust measurement values of various thrust models, with (a) depicting thrust without temperature compensation. During operation, the airflow from the rotor directed towards the BFS led to a decrease in sensor temperature (a decrease of 1.5℃), resulting in unstable readings.

In (a), the curve exhibits a distinct downward trend, indicating unstable readings, ultimately reduced by 1.5N. (b) illustrates thrust without weight compensation, falling significantly short of the desired thrust by a substantial difference value (2.51N). In (c), the curve demonstrates thrust without friction force compensation, slightly below the desired thrust with a difference value of 1.09N. (d) depicts thrust with temperature, weight, and friction force compensation, closely matching the desired thrust (0.02N).

Table V reveals that the highest variance observed in model I suggests a significant impact of temperature on the stability of sensor measurements. Additionally, models II and III exhibit larger errors, highlighting the substantial influence of weight and friction force on measurement accuracy. Conversely, model (11) demonstrates minimal variance and error, indicating superior measurement stability and accuracy. Hence, temperature compensation can enhance measurement stability, whereas weight and friction force compensation improve measurement accuracy.

D. Single-axis Dynamical Testing Platform

To validate the feasibility of the BFS for thrust measurement and force feedback control, we constructed a single-axis dynamical testing platform, as illustrated in Fig. 12, where the flight controller is used to collect the thrust measured from BFS, perform Kalman filtering processing and thrust feedback control. One end of the arm secures the BFS, while the other end is connected to the hinge. The hinge restricts the arm's rotational motion to the XOZ plane and limits it to ±30° to ensure experiment safety. Finally, these structures are affixed to the pedestal to enhance the stability of the testing platform.

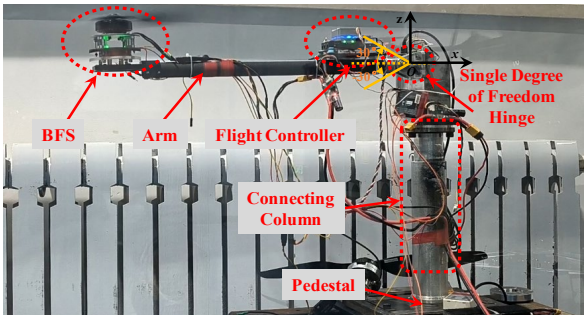

Fig. 12. Schematic of the testing platform.

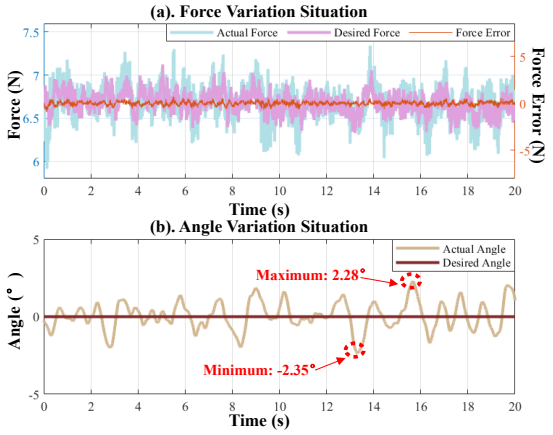

Fig. 13. Situation of force and angle variation during force feedback.

A closed-loop control experiment was performed to maintain the arm horizontal, corresponding to a desired rotation angle of 0° in the XOZ plane. Fig. 13 shows the situation of the force and angle during force closed-loop control. In (a), the left Y-axis represents actual and desired forces, demonstrating that the actual force closely tracks changes in the desired force; the right Y-axis shows the force error curve, representing the difference between actual and desired forces. The maximum error value less than 0.1N indicates the high control accuracy achievable with this mounting structure incorporating the BFS. In (b), once the system stabilizes, the rotation angle remains within the range of ±3°, indicating its stability during the closed-loop force control process. In conclusion, the results confirm the stability and accuracy of force output, demonstrating the feasibility of utilizing the BFS for thrust measurement and force feedback control on the multi-rotor UAV platform.

V. Conclusions and Future Work

In this study, a low-cost and lightweight barometric force sensor (BFS) was designed to directly measure the thrust generated by the rotor. We designed the construction of the BFS to ensure an adequate measurement range, and developed its parameter model. We devised a stability improvement strategy to mitigate the impact of temperature on the BFS. Following that, we designed the mounting structure to convert tensile forces acting on the BFS into pressure for its protection, and conducted an analysis on the effects of weight and friction force on thrust measurement to refine the thrust model. Additionally, we verified that the BFS has adequate bandwidth to accommodate UAV thrust variations. Finally, the constructed single-axis dynamical system confirmed the feasibility of integrating the BFS onto UAV for thrust measurement and force feedback control.

In future work, we aim to construct a multirotor UAV equipped with a thrust feedback control system to accomplish highly maneuverable operations and validate the enhancement in performance under wind disturbance conditions.

References

[1] Darvishpoor, Shahin, et al, "Configurations, flight mechanisms, and applications of unmanned aerial systems: A review," *Prog. Aerosp. Sci.*, 2020.

[2] Hassanalian, Mostafa, and Abdessattar Abdelkefi, "Classifications, applications, and design challenges of drones: A review," *Prog. Aerosp. Sci.*, pp. 99-131, 2017.

[3] Z. Wei, Z. Meng, M. Lai, H. Wu, J. Han and Z. Feng, "Anti-Collision Technologies for Unmanned Aerial Vehicles: Recent Advances and Future Trends," *IEEE Internet Things J.*, vol. 9, no. 10, pp. 7619-7638, May 2022.

[4] Y. Xie, X. Yu, Y. Shi and L. Guo, "SPT-Based Composite Hierarchical Antidisturbance Control Applied to a Quadrotor UAV," *IEEE Trans. Ind. Electron.*, vol. 70, no. 1, pp. 635-645, 2023.

[5] Wang, Yin, and Daobo Wang, "Variable thrust directional control technique for plateau unmanned aerial vehicles," *Sci. China Inf. Sci.*, vol. 59, no. 3, pp. 33201-1, 2016.

[6] M. Bangura and R. Mahony, "Thrust Control for Multirotor Aerial Vehicles," *IEEE Trans. Rob.*, vol. 33, no. 2, pp. 390-405, April 2017.

[7] M. Bangura, M. Melega, R. R. Naldi, and R. Mahony, "Aerodynamics of rotor blades for quadrotors," *arXiv:1601.00733*, pp. 11773–11780, 2016.

[8] H. Jeon, J. Song, H. Lee and Y. Eun, "Modeling Quadrotor Dynamics in a Wind Field," *IEEE/ASME Trans. Mechatron.*, vol. 26, no. 3, pp. 1401-1411, June 2021.

[9] J. Svacha, K. Mohta and V. Kumar, "Improving quadrotor trajectory tracking by compensating for aerodynamic effects," *2017 International Conference on Unmanned Aircraft Systems (ICUAS)*, Miami, FL, USA, pp. 860-866, 2017.

[10] A. Letalenet and P. Morin, "Identification and evaluation of a force model for multirotor UAVs," *2020 IEEE International Conference on Robotics and Automation (ICRA)*, Paris, France, pp. 4280-4286, 2020.

[11] Bauersfeld, Leonard, et al, "Neurobem: Hybrid aerodynamic quadrotor model," *arXiv:2106.08015*, 2021.

[12] Smith, Christopher, and Alok Sinha, "Time Varying Rotor Aerodynamics for Quadrotor Vehicles," *AIAA SCITECH 2023 Forum.*, 2023.

[13] Werner, Lennart, et al, "Thrust vector observation for force feedback-controlled UAVs," *Drones.*, vol. 6, no. 2, 2022.

[14] Marchman, Christopher Scott, "Thrust sensing for small UAVs," *Missouri University of Science and Technology*, 2016.

[15] Kamp, R, "Design of a mechanical-based thrust sensing unit for multi-rotor UAVs," *BS thesis. University of Twente*, 2018.

[16] Gong, Andrew, Hugh Maunder, and Dries Verstraete, "Development of an in-flight thrust measurement system for UAVs," *53rd AIAA/SAE /ASEE Joint Propulsion Conference*, 2017.

[17] JR3 Team, "Jr3: Multi-axis load cell technologies," [Online]. *Available: http://www.jr3.com/*, no. 7, 2016.

[18] Guggenheim, Jacob W., et al, "Robust and inexpensive six-axis force–torque sensors using MEMS barometers," *IEEE/ASME Trans. Mechatron.*, vol. 22, no. 2, pp. 838-844, 2017.

[19] Y. Tenzer, L. P. Jentoft and R. D. Howe, "The Feel of MEMS Barometers: Inexpensive and Easily Customized Force Array Sensors," *IEEE Rob. Autom. Mag.*, vol. 21, no. 3, pp. 89-95, Sept. 2014.

[20] T. De Clercq, A. Sianov and G. Crevecoeur, "A Soft Barometric Force Sensor to Simultaneously Localize Contact and Estimate Normal Force With Validation to Detect Slip in a Robotic Gripper," *IEEE Rob. Autom. Lett.*, vol. 7, no. 4, pp. 11767-11774, Oct. 2022.

[21] R. Kõiva, T. Schwank, G. Walck, M. Meier, R. Haschke and H. Ritter, "Barometer-based Tactile Skin for Anthropomorphic Robot Hand," *2020 IEEE/RSJ International Conference on Intelligent Robots and Systems (IROS)*, Las Vegas, NV, USA, pp. 9821-9826, 2020.

[22] X. Zhou and A. J. Spiers, "Force Identification of Object Shapes via In-Hand Manipulation with A Minimalistic Barometric Force Sensor Array," *2023 IEEE International Conference on Robotics and Automation (ICRA)*, London, United Kingdom, pp. 12590-12596, 2023.

[23] M. Y. M. Chuah, L. Epstein, D. Kim, J. Romero and S. Kim, "Bi-Modal Hemispherical Sensor: A Unifying Solution for Three Axis Force and Contact Angle Measurement," *2019 IEEE/RSJ International Conference on Intelligent Robots and Systems (IROS)*, Macau, China, 2019.

[24] Davis, Edwin, and P. Pounds, "Direct thrust and velocity measurement for a micro UAV rotor," *Proc. Australas. Conf. Robot. Autom.*, 2016.

[25] E. Davis and P. E. I. Pounds, "Direct Sensing of Thrust and Velocity for a Quadrotor Rotor Array," *IEEE Rob. Autom. Lett.*, vol. 2, no. 3, pp. 1360-1366, July 2017.

[26] Semiconductor Freescale. "MPL115A2 Miniature I^2C Digital Barometer," *Datasheet*.